JOURNAL OF GUIDANCE, CONTROL, AND DYNAMICS
Vol. 31, No. 2, March–April 2008

Structural Dynamics of Spin-Stabilized Solar Sails with Applications to UltraSail

Thierry Botter,* Victoria L. Coverstone,† and Rodney L. Burton‡
University of Illinois at Urbana–Champaign, Urbana, Illinois 61801

DOI: 10.2514/1.27609

The sail dynamics of spin-stabilized solar sail designs are examined in this paper. The nonlinear governing equations of motion are derived for four different and progressively more complex dynamical scenarios: pitch (one dimensional); pitch and sweepback (two dimensional); pitch and lead/lag (two dimensional); and pitch, sweepback, and lead/lag (three dimensional). These equations are applied to UltraSail, a novel solar sail design developed at the University of Illinois at Urbana–Champaign, which relies on small-tip satellites to provide tension in rectangular sails. Steady-state and time-dependent characteristics are numerically calculated and discussed. Properties such as the spacecraft acceleration are predicted, and transient sail responses to an applied perturbation are simulated. Results place UltraSail as a strong candidate for future solar sail missions with performance challenging previously proposed concepts.

Nomenclature

$A, B, O, S, \sim$	=	reference frames
a_z	=	acceleration away from the Sun, m/s^2
c	=	sail chord, m
$\bar{c}$	=	pitch-wave speed, m/s
F	=	applied force
L	=	sail length, m
M_{hub}	=	mass of the hub, kg
m_{sail}	=	mass of each coated sail, kg
m_{sat}	=	mass of the tip satellite, kg
N	=	number of blades
P_{solar}	=	actual solar pressure acting on sail, Pa
P_{o}	=	solar pressure at a distance of 1 AU, Pa
T	=	spin period
$\bar{T}$	=	tension by tip satellite/cross-sectional area, Pa
t	=	time coordinate
$\bar{t}$	=	sail thickness, μm
$\bar{x}_O$	=	separation between the hub end of the sail and the spin axis, m
x, y, z	=	Cartesian coordinates
Y	=	Young's modulus
α	=	viscous damping constant
β	=	angular displacement because of lead/lag, relates reference frames O and A
ε	=	elastic strain
θ	=	pitch angle, relates reference frames $\sim$ and S
ζ	=	sweepback angle, relates reference frames S and B
ρ	=	coated sail density, kg/m^3
σ	=	stress density = tension/cross-sectional area, Pa
ϕ	=	lead/lag angle, relates reference frames B and O
ω	=	spin angular velocity

Received 16 September 2006; accepted for publication 5 July 2007.

*Graduate Student, Department of Aerospace Engineering, 104 South Wright Street; t_botter@hotmail.com. Student Member AIAA.

†Professor, Department of Aerospace Engineering, 104 South Wright Street; vcc@uiuc.edu. Associate Fellow AIAA.

‡Professor, Department of Aerospace Engineering, 104 South Wright Street; rburton@uiuc.edu. Associate Fellow AIAA.

Introduction

SOLAR sails are a relatively new form of space propulsion; the technology was first legitimately considered for a space mission in the 1970s. Various designs were proposed at the time, but none were realized because they were deemed overly ambitious. Strong research in the field finally emerged during the 1990s, which led to the construction of several prototypes. To date, only two successful space-based sail deployment tests have taken place: a 2-m film structure in 1993 as part of Progress M-15 and two 7.5 μm-thick sails in 2004 during a mission led by the Japanese space agency.

The fundamental concept behind all solar sail designs is the use of momentum flux from solar photons to produce thrust. Other common features include the need for strong yet thin reflective films, a control system, a lightweight support structure, and a large sail area to maximize the thrust or payload ratio. Unlike conventional chemical propulsion, solar sails have low thrust levels with currently feasible accelerations on the order of 0.1 to 0.25 mm/s^2 at 1 AU [1]. However, over large time periods, they can theoretically reach far greater speeds than what is currently possible [2]. Also, solar sails are arguably the most efficient method of space travel, because they require no onboard fuel for their main propulsion system.

To date, two methods have been proposed for the stabilization of the sails: spin stabilization or three-axis stabilization. Both rely on the inherent rigidity of a support structure. In the latter case, sails are supported using long booms, much like a kite. It is also possible to couple the booms with masts, stays, and cables to form a parachutelike design, which reduces load on the booms and the weight of the structure at the expense of more complexity. As for spin stabilization, sails are stiffened by spinning about a central hub. This approach can lead to high propulsive efficiencies without strong compressive mast loads [3]. Two distinct concepts have been introduced using this technique: a circular-disk-shaped sail and the Heliogyro, consisting of a series of rectangular blades equally spaced around the central hub, in a similar fashion to a helicopter rotor. Keeping with the helicopter analogy, the blades of the Heliogyro can be tilted to control the direction of the solar pressure force and thus maneuver the spacecraft.

A joint University of Illinois–CU Aerospace research group has been investigating UltraSail [4], an ultralightweight, spinning solar sail concept conceived by R. L. Burton. The design relies on extremely thin films for propulsion, and does not contain booms or masts. These features significantly reduce the structural mass, rendering UltraSail capable of high payload fractions and accelerations. Tension in the sail blades is provided by spinning the film mass and microsatellites located at the blade tips.

The microsatellites fulfill a second function by controlling the sail pitch. Using small onboard thrusters, the tip satellites induce a pitch

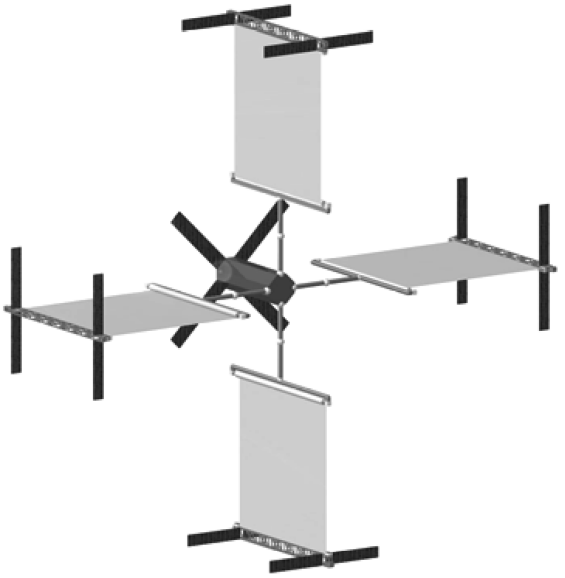

Fig. 1 Conceptual drawing of UltraSail [2].

angle in the blades, changing the incidence angle of the incoming photons, inducing a torque on the blades that impacts both the orientation of the spacecraft and its trajectory. By coordinating the motion of the individual tip satellites, in a manner similar to formation flying, it is possible to maneuver and control the orientation of UltraSail [5]. A conceptual drawing of UltraSail is found in Fig. 1.

In this paper, the underlying mathematics for the blade shape and motion of spin-stabilized solar sails is developed. Four different cases are examined: pitch only (1-D); pitch and sweepback (2-D); pitch and lead/lag (2-D); and pitch, sweepback, and lead/lag (3-D). Certain characteristics of UltraSail, such as its acceleration and the deflection of its blades under steady-state conditions, are analytically modeled. These conditions, along with others, both time dependent and independent, are also numerically simulated using the UltraSail baseline-design parameters. Particular emphasis is placed on the response of sails to pitch controls applied at their end. Various boundary conditions in pitch, both at the hub and the tip satellites, are investigated.

Theory

Frames of Reference

Before outlining the mathematical equations that govern the sails, it is important to define certain frames of reference and their nomenclature. To fully and accurately model the motion of the sails, five reference frames are needed. Each frame is included to highlight a different physical characteristic of the blades: pitch, sweepback, lead/lag deflection, steady-state spin, and acceleration away from the Sun. These characteristics are defined as follows:

1) Pitch (θ): angular displacement of the blade about its longitudinal axis, at the midchord.

2) Sweep back (ζ): deflection away from the Sun (rearward deflection) because of solar pressure.

3) Steady-state spin (ω): steady-state rotational velocity of the blade about the central hub.

4) Lead/lag (ϕ, β): deflection of the sail in the spin plane; deflection in the direction of spin = lead,
deflection in the opposite direction of spin = lag.

5) Acceleration (a_z): linear acceleration of the spacecraft center of mass away from the Sun created by the solar photon momentum flux.

A description of each reference frame is provided in Table 1. These descriptions are complemented by a flow chart, Fig. 2, which orders the frames from most local to most global and indicates the link between each successive one. Finally, to visually represent the properties of the frames of reference and their interrelations, schematics of all five frames are included in Figs. 3–5.

Table 1 Description of all five reference frames

Symbol	Location of origin	Direction of axes
$\sim$	Individual points along the sail midchord	$\tilde{x}$ = surface length $\tilde{y}$ = surface chord $\tilde{z}$ = outward normal
S	Individual points along the sail midchord	x_S coincides with $\tilde{x}$ $y_S = \tilde{y}$ direction when $\theta = 0$ deg $z_S = \tilde{z}$ direction when $\theta = 0$ deg
B	Individual points along the sail midchord	$x_B = x_S$ direction when $\zeta = 0$ deg y_B coincides with y_S $z_B = z_S$ direction when $\zeta = 0$ deg
O	Center of the hub	$x_O = x_B$ direction when $\varphi = 0$ deg $y_O = y_B$ direction when $\varphi = 0$ deg z_O coincides with z_B
A	Center of the Sun (inertial, spacecraft-facing reference frame)	$y_A = y_O$ direction when $\beta = 0$ deg z_A coincides with z_O (always pointing towards the solar sail)

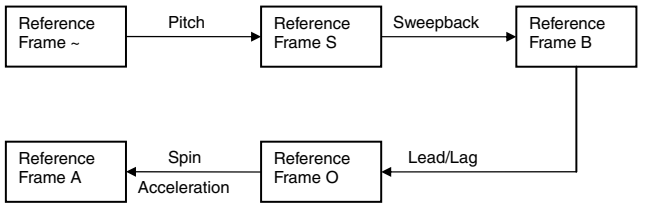

Fig. 2 Flow chart outlining the five reference frames and the link between each successive one.

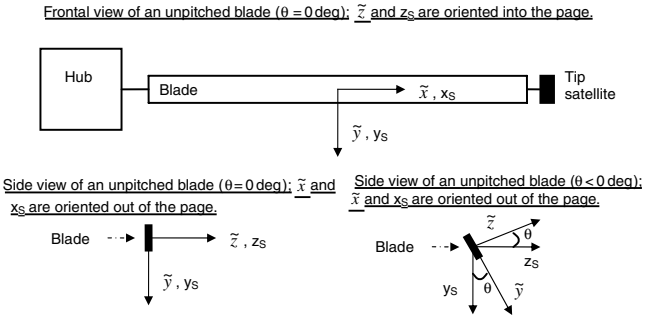

Fig. 3 Diagram of reference frames $\sim$ and *S*. Objects are not set to scale.

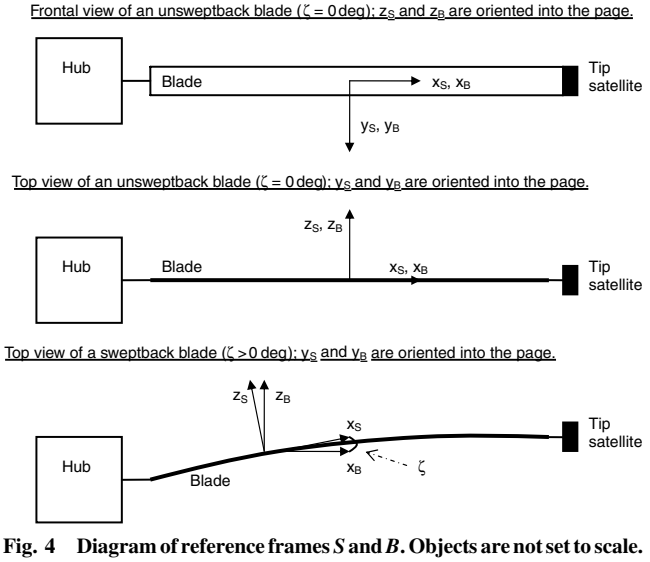

Fig. 4 Diagram of reference frames *S* and *B*. Objects are not set to scale.

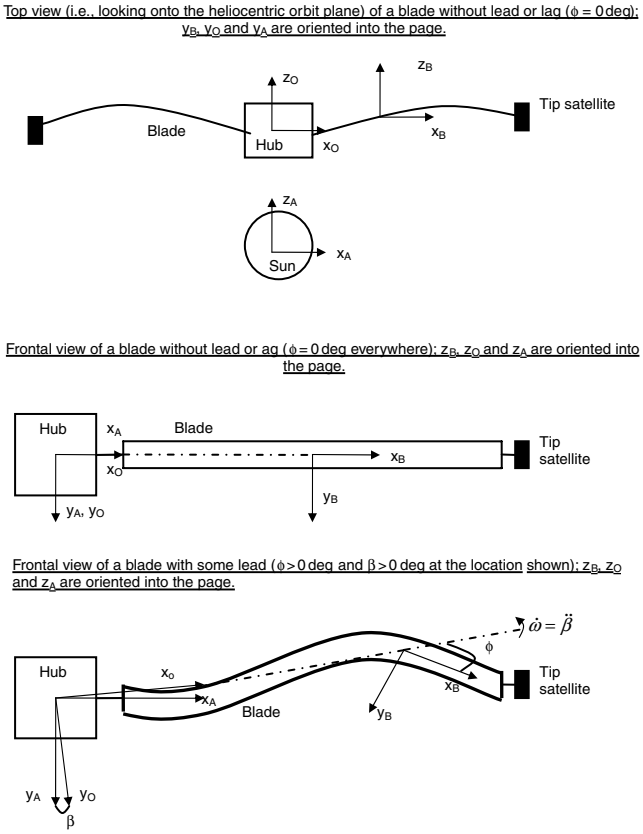

Fig. 5 Diagram of reference frames *B*, *O*, and *A*. Objects are not set to scale.

Force Balance Equation

The approach taken to derive the general, governing equation for the sail blade shape and motion is similar to that of MacNeal [5,6]. However, fewer assumptions are made, rendering more accurate, nonlinear equations. This paper thus extends past work on spin-stabilized solar sails. It also differs from other analyses of the nonlinear solar sail motion, such as Salama and Trubert [7], by considering Newton's second law instead of Hamilton's variational principle.

Applying structural mechanics principles to a small sail element produces a force balance equation. The differential stress forces, along with the solar pressure force, are summed to determine the global acceleration $\boldsymbol{a}$ of the small element under consideration:

$$\frac{\partial}{\partial\tilde{x}}(\sigma_{\tilde{x}}\cdot\hat{\tilde{\boldsymbol{x}}})+\frac{\partial}{\partial\tilde{y}}(\sigma_{\tilde{y}}\cdot\hat{\tilde{\boldsymbol{y}}})+\frac{P_{\text{solar}}}{\bar{t}}\cdot\hat{\tilde{\boldsymbol{z}}}=\rho\cdot\boldsymbol{a} \tag{1}$$

The unit vectors are directed along the normal and tangential directions at every point along the midchord. Equation (1) was applied to every case studied in this research and will be further developed in the following sections, as each case is considered individually.

To simplify the force balance equation, a common set of approximations can be applied to every case study. After a careful review of the problem and its premise, three such simplifications were selected. All are expected to have a minimal impact on the accuracy of the simulated sail motion.

1) Extremely thin materials under light loading, such as spin-stabilized solar sails on the order of 1–10 μm [1,8] thickness, have negligible bending stiffness. Chordwise properties of such sails mostly result from the competition between tensile stress, which flattens them, and solar pressure, which tends to furl them about their midchord. Because the calculated ratio of tensile stress to solar pressure is approximately 10^9, the sail blades are assumed to remain flat (i.e., constant θ over the chord) and carry a uniform and constant stress over their chord. In other words, the sails are treated as one-dimensional membranes, a model supported by past work [9], (see "Simulations and Results").

2) With typical near-term solar sail materials, UltraSail blades would experience a strain on the order of 10^{-5}. Consequently, elastic deformations are neglected.

3) Because this paper focuses on blade movements over short time periods (up to 3000 s), the spacecraft (not the blades) is assumed to constantly face the Sun and remain near a distance of 1 AU from the Sun. Furthermore, solar pressure is taken to be constant and uniform over the sail area.

Additionally, the interdependence between the blades and the hub was ignored. Because the study was focused on examining the motion of single blades, it was deemed more appropriate to neglect this interdependence. Of course, the actual, overall motion of UltraSail is intimately dependent on the interaction between the blades and the hub.

Pitch-Only Case

The first and simplest case examined is the time-dependent variation in pitch of a constantly straight and flat blade; both ζ and ϕ are assumed to remain equal to 0 deg. Equation (1) must be expanded and transformed to capture this variation in pitch angle, θ, within a single, unifying equation.

First, unit vectors are replaced by variables. Because pitch relates the reference frames S and $\sim$, and that pitch causes a deflection in z_s, the terms of Eq. (1) are best evaluated along the z_s direction. Applying this projection transforms the unit vectors $\hat{\tilde{\boldsymbol{x}}}$ and $\hat{\tilde{\boldsymbol{y}}}$ into partial differential terms:

$$\frac{\partial}{\partial\tilde{x}}\left(\sigma_{\tilde{x}}(\tilde{x})\cdot\frac{\partial z_S(\tilde{x},\tilde{y},t)}{\partial\tilde{x}}\right)+\frac{\partial}{\partial\tilde{y}}\left(\sigma_{\tilde{y}}(\tilde{x},\tilde{y})\cdot\frac{\partial z_S(\tilde{x},\tilde{y},t)}{\partial\tilde{y}}\right)+\frac{P_{\text{solar}}}{\bar{t}}\cdot(\hat{\tilde{\boldsymbol{z}}}\cdot\hat{z}_S)=\rho\cdot(\boldsymbol{a}\cdot\hat{z}_S) \tag{2}$$

As for $\hat{\tilde{\boldsymbol{z}}}$, it is replaced by the trigonometric expression for its projection onto $\hat{z}_S$: $\cos[\theta(\tilde{x},t)]$. The remaining vector, $\boldsymbol{a}$, and its projection are handled through relative motion.

Starting with the position vector of a small sail element in the $\sim$ reference frame, the global acceleration of this element, observed in the A reference frame, is obtained by applying the equation for relative acceleration four consecutive times, one for each bridge between two successive reference frames (see Fig. 2). The resulting, global acceleration components, taken along the axes of the O reference frame (hence the O/A subscript), are

$$\ddot{x}_{O/A}=\ddot{x}_O(\tilde{x},t)-2\cdot\omega\cdot\tilde{y}\cdot\sin[\theta(\tilde{x},t)]\cdot\frac{\partial\theta(\tilde{x},t)}{\partial t}-\omega^2\cdot x_O(\tilde{x},t) \tag{3}$$

$$\ddot{y}_{O/A}=-\tilde{y}\cdot\left\{\cos[\theta(\tilde{x},t)]\cdot\left(\frac{\partial\theta(\tilde{x},t)}{\partial t}\right)^2+\sin[\theta(\tilde{x},t)]\cdot\frac{\partial^2\theta(\tilde{x},t)}{\partial t^2}\right\}-2\cdot\omega\cdot\dot{x}_O(\tilde{x},t)-\omega^2\cdot\tilde{y}\cdot\cos[\theta(\tilde{x},t)] \tag{4}$$

$$\ddot{z}_{O/A}=\ddot{z}_O(\tilde{x},t)+a_z+\tilde{y}\cdot\left\{-\sin[\theta(\tilde{x},t)]\cdot\left(\frac{\partial\theta(\tilde{x},t)}{\partial t}\right)^2+\cos[\theta(\tilde{x},t)]\cdot\frac{\partial^2\theta(\tilde{x},t)}{\partial t^2}\right\} \tag{5}$$

The components are dependent on both time, symbolized by t, and two-dimensional space, represented by the variables $\tilde{x}$ and $\tilde{y}$. As an independent variable, $\tilde{x}$ indicates the midchord point under consideration for several other variables. Variables containing the subscript O are measured with respect to the axes of O as observed in O.

Because the sail blade is assumed to vary only in pitch, z_s coincides with z_O, and there is no translational motion (i.e.,

$\ddot{x}_O = \dot{x}_O = \ddot{z}_O = 0$). Thus, the acceleration component along $\hat{z}_s$ will be a modified version of $\ddot{z}_{O/A}$ given in Eq. (5):

$$\boldsymbol{a} \cdot \hat{\boldsymbol{z}}_S = a_z + \tilde{y} \cdot \left[-\sin[\theta(\tilde{x}, t)] \cdot \left(\frac{\partial \theta(\tilde{x}, t)}{\partial t} \right)^2 + \cos[\theta(\tilde{x}, t)] \cdot \frac{\partial^2 \theta(\tilde{x}, t)}{\partial t^2} \right] \tag{6}$$

The applied solar pressure, P_{solar}, is related to the nominal solar pressure at 1 AU. Because the applied pressure is always normal to the sail and the nominal pressure points linearly away from the Sun, both are related by the trigonometric relation:

$$P_{\text{solar}} = P_O \cdot \cos^2[\theta(\tilde{x}, t)] \tag{7}$$

The remaining unknown, $\sigma_{\tilde{y}}(\tilde{x}, \tilde{y})$, is handled by considering the projection of Eq. (1) onto $\hat{\tilde{y}}$. Equations (4) and (5) provide the basis to properly project the acceleration:

$$\frac{\partial}{\partial \tilde{y}}[\sigma_{\tilde{y}}(\tilde{x}, \tilde{y})] = \rho \cdot \{\ddot{y}_{O/A} \cdot \cos[\theta(\tilde{x}, t)] + \ddot{z}_{O/A} \cdot \sin[\theta(\tilde{x}, t)]\} \tag{8}$$

Integrating both sides of Eq. (8) with respect to $\tilde{y}$ yields the general equation stress along the chord:

$$\sigma_{\tilde{y}}(\tilde{x}, \tilde{y}) = \rho \cdot \left\{ -\frac{\tilde{y}^2}{2} \cdot \left[\left(\frac{\partial \theta(\tilde{x}, t)}{\partial t} \right)^2 + \omega^2 \cdot \cos^2[\theta(\tilde{x}, t)] \right] + \tilde{y} \cdot a_z \cdot \sin[\theta(\tilde{x}, t)] \right\} \tag{9}$$

A final reduction is made to eliminate the chordwise dependence, $\tilde{y}$, and isolate θ. Because pitch, pressure, and stress are assumed to be uniform along the chord, the sum of their moments about the midchord is zero. The modified form of Eq. (2) is therefore converted into a momentlike equation. Both sides of the governing equation are multiplied by $\tilde{y}$ and then integrated from one edge of the chord to the other:

$$\int_{-c/2}^{c/2} \mathrm{d}\tilde{y} \cdot \tilde{y} \cdot \left\{ \frac{\partial}{\partial \tilde{x}} \left(\sigma_{\tilde{x}}(\tilde{x}) \cdot \frac{\partial}{\partial \tilde{x}} \{\tilde{y} \cdot \sin[\theta(\tilde{x}, t)]\} \right) + \frac{\partial}{\partial \tilde{y}} \left(\sigma_{\tilde{y}}(\tilde{x}, \tilde{y}) \cdot \frac{\partial}{\partial \tilde{y}} \{\tilde{y} \cdot \sin[\theta(\tilde{x}, t)]\} \right) + \frac{P_O}{\tilde{t}} \cdot \cos^3[\theta(\tilde{x}, t)] \right\} = \int_{-c/2}^{c/2} \mathrm{d}\tilde{y} \cdot \tilde{y} \cdot \rho \cdot \left\{ a_z + \tilde{y} \cdot \left[-\sin[\theta(\tilde{x}, t)] \cdot \left(\frac{\partial \theta(\tilde{x}, t)}{\partial t} \right)^2 + \cos[\theta(\tilde{x}, t)] \cdot \frac{\partial^2 \theta(\tilde{x}, t)}{\partial t^2} \right] \right\} \tag{10}$$

Several terms are eliminated by this procedure, including the differential terms in $\tilde{y}$, P_{solar} and a_z. The final form of the governing equation for the sail motion is that of a damped-wave equation:

$$\rho \cdot \cos[\theta(\tilde{x}, t)] \cdot \frac{\partial^2 \theta(\tilde{x}, t)}{\partial t^2} + \sigma_{\tilde{x}}(\tilde{x}) \cdot \sin[\theta(\tilde{x}, t)] \cdot \left(\frac{\partial \theta(\tilde{x}, t)}{\partial \tilde{x}} \right)^2 - \sigma_{\tilde{x}}(\tilde{x}) \cdot \cos[\theta(\tilde{x}, t)] \cdot \frac{\partial^2 \theta(\tilde{x}, t)}{\partial \tilde{x}^2} + \rho \cdot \omega^2 \cdot \sin[\theta(\tilde{x}, t)] \cdot \cos^2[\theta(\tilde{x}, t)] - \frac{\partial \sigma_{\tilde{x}}(\tilde{x})}{\partial \tilde{x}} \cdot \cos[\theta(\tilde{x}, t)] \cdot \frac{\partial \theta(\tilde{x}, t)}{\partial \tilde{x}} = 0 \tag{11}$$

Equation (11) is the nonlinear equivalent of the equation found by MacNeal [5,6] for the Heliogyro. Because it assumes the blades remain relatively straight and flat, its validity is proportional to the spin angular velocity: the faster the solar sail rotates, the more tension is generated in the blades and the more accurate the pitch-only model.

Pitch and Sweepback Case

The second situation studied considers coupling between sweepback and pitch during both steady-state and transitive motion. A logical extension of the previous section, this case no longer assumes that the blade is flat, but rather has a varying rearward deflection because of the solar pressure force. A new angle, ζ, is included in the derivation to represent this nonlinear deflection.

Steps taken to derive the governing equation for θ in this situation are identical to those mentioned in the past section. Although a new variable is present, the results are closely related to those obtained for the pitch-only case. The most notable changes caused by ζ are on the acceleration components and the expression for P_{solar}. For instance, the relation between P_{solar} and P_o is now a product of cosines:

$$P_{\text{solar}} = P_O \cdot \cos^2[\theta(\tilde{x}, t)] \cdot \cos^2[\zeta(\tilde{x}, t)] \tag{12}$$

The angle ζ also impacts the position components x_O and z_O by allowing them to vary over time. Strictly speaking, this would consequently produce a small time-dependent variation in $\sigma_{\tilde{x}}$. However, the approximations stated earlier continue to apply and thus stresses in the sail are assumed to remain constant. The final result for the governing equation also has the form of a damped-wave equation:

$$\rho \cdot \cos[\theta(\tilde{x}, t)] \cdot \frac{\partial^2 \theta(\tilde{x}, t)}{\partial t^2} + \sigma_{\tilde{x}}(\tilde{x}) \cdot \sin[\theta(\tilde{x}, t)] \cdot \left(\frac{\partial \theta(\tilde{x}, t)}{\partial \tilde{x}} \right)^2 - \sigma_{\tilde{x}}(\tilde{x}) \cdot \cos[\theta(\tilde{x}, t)] \cdot \frac{\partial^2 \theta(\tilde{x}, t)}{\partial \tilde{x}^2} + \rho \cdot \omega^2 \cdot \sin[\theta(\tilde{x}, t)] \cdot \cos^2[\theta(\tilde{x}, t)] \cdot \cos^2[\zeta(\tilde{x}, t)] - \frac{\partial \sigma_{\tilde{x}}(\tilde{x})}{\partial \tilde{x}} \cdot \cos[\theta(\tilde{x}, t)] \cdot \frac{\partial \theta(\tilde{x}, t)}{\partial \tilde{x}} - \rho \cdot \sin[\theta(\tilde{x}, t)] \cdot \cos^2[\theta(\tilde{x}, t)] \cdot \left(\frac{\partial \zeta(\tilde{x}, t)}{\partial t} \right)^2 - 2\rho \cdot \omega \cdot \cos[\theta(\tilde{x}, t)] \cdot \sin^2[\theta(\tilde{x}, t)] \cdot \cos[\zeta(\tilde{x}, t)] \cdot \frac{\partial \zeta(\tilde{x}, t)}{\partial t} = 0 \tag{13}$$

Two additional equations are necessary to fully model the sail motion. The first stems from projecting Eq. (1) onto the z_O axis as observed in the frame of reference A, and evaluating its momentlike equation. Because $\sigma_{\tilde{y}}(\tilde{x}, \tilde{y})$ is symmetric about the midchord, terms with $\tilde{y}$ drop, leaving behind

$$\rho \cdot \ddot{z}_{O/A}|_{\tilde{y}=0} = \rho \cdot [\ddot{z}_O(\tilde{x}, t) + a_z] = \frac{\partial}{\partial \tilde{x}} \{\sigma_{\tilde{x}}(\tilde{x}) \cdot \sin[\zeta(\tilde{x}, t)]\} + \frac{P_{\text{solar}}}{\tilde{t}} \cdot \cos[\theta(\tilde{x}, t)] \cdot \cos[\zeta(\tilde{x}, t)] \tag{14}$$

Equation (14) corresponds to the nonlinear out-of-plane dynamics. Unlike other similar works [3,5,6], it accounts for small angles and the linear acceleration experienced by a Sun-facing solar sail.

The second additional equation is merely the mathematical definition of ζ:

$$\sin[\zeta(\tilde{x}, t)] = \frac{\partial z_O(\tilde{x}, t)}{\partial \tilde{x}} \tag{15}$$

Together, Eqs. (13–15) form a coupled set of equations that determine the blade position over space and time for the pitch and sweepback case.

Pitch and Lead/Lag Case

An alternate logical extension of the pitch-only analysis is the coupling between pitch and lead/lag on the blade motion. In this case, the sail is allowed to experience a space and time-dependent increase in spin, while maintaining a constant rearward deflection in time. As with the pitch and sweepback case, new angle terms are added to express the deflection of the sail in the spin plane: ϕ and β.

Again, the same steps as for the pitch-only case are taken to obtain the governing equation for θ. The addition of ϕ and β in this third case impacts a number of terms, most notably ω, which becomes space and time dependent. Also, y_A, the projection of a midchord point along the y_A axis, replaces z_O as the second time-dependent spatial coordinate. Despite these changes, the governing equation for θ still has the form of a damped-wave equation:

$$\rho\cdot\cos[\theta(\tilde{x},t)]\cdot\frac{\partial^2\theta(\tilde{x},t)}{\partial t^2}+\sigma_{\tilde{x}}(\tilde{x})\cdot\sin[\theta(\tilde{x},t)]\cdot\left(\frac{\partial\theta(\tilde{x},t)}{\partial\tilde{x}}\right)^2-\sigma_{\tilde{x}}(\tilde{x})\cdot\cos[\theta(\tilde{x},t)]\cdot\frac{\partial^2\theta(\tilde{x},t)}{\partial\tilde{x}^2}+\rho\cdot\cos[\theta(\tilde{x},t)]\cdot\sin[\zeta(\tilde{x})]\frac{\partial^2\phi(\tilde{x},t)}{\partial t^2}-\rho\cdot\cos[\theta(\tilde{x},t)]\cdot\sin[\zeta(\tilde{x})]\frac{\partial\omega(\tilde{x},t)}{\partial t}-2\rho\cdot\omega(\tilde{x},t)\cdot\sin[\theta(\tilde{x},t)]\cdot\cos^2[\theta(\tilde{x},t)]\cdot\cos^2[\zeta(\tilde{x})]\cdot\frac{\partial\phi(\tilde{x},t)}{\partial t}+\rho\cdot[\omega(\tilde{x},t)]^2\cdot\sin[\theta(\tilde{x},t)]\cdot\cos^2[\theta(\tilde{x},t)]\cdot\cos^2[\zeta(\tilde{x})]-\frac{\partial\sigma_{\tilde{x}}(\tilde{x})}{\partial\tilde{x}}\cdot\cos[\theta(\tilde{x},t)]\cdot\frac{\partial\theta(\tilde{x},t)}{\partial\tilde{x}}=0 \tag{16}$$

Three additional equations are required to fully capture the two-dimensional motion. Similar to the past scenario, the momentlike form of the force balance equation along the y_O axis, as observed in the frame of reference A, constitutes one necessary addition:

$$\rho\cdot\ddot{y}_{O/A}|_{\tilde{y}=0}=\frac{\partial}{\partial\tilde{x}}[\sigma_{\tilde{x}}(\tilde{x})\cdot\cos(\zeta)\cdot\sin(\phi)]-\frac{P_{\text{solar}}}{\bar{t}}\cdot[\cos(\phi)\cdot\sin(\theta)+\sin(\zeta)\cdot\sin(\phi)\cdot\cos(\theta)] \tag{17}$$

Equation (17) describes the nonlinear in-plane blade deflection dynamics. Applying small-angle approximations reduces the equation to more common linear forms [3,5,6], minus the contribution of material stiffness because of this paper's second assumption.

The acceleration component $\ddot{y}_{O/A}$ evaluated at the midchord is obtained from relative acceleration theory, as in Eq. (3):

$$\ddot{y}_{O/A}|_{\tilde{y}=0}=\ddot{y}_{O/A}(\tilde{x},0,t)=-x_O(\tilde{x},t)\cdot\ddot{\beta}(\tilde{x},t)-2\cdot\omega(\tilde{x},t)\cdot\dot{x}_O(\tilde{x},t) \tag{18}$$

By definition, β is related to ω through the relation

$$\dot{\beta}(\tilde{x},t)=\omega(\tilde{x},t) \tag{19}$$

The principal definition of β forms the third governing equation:

$$\sin[(\beta(\tilde{x},t)]=-\frac{y_A(\tilde{x},t)}{x_O(\tilde{x},t)} \tag{20}$$

The fourth and final equation is obtained from the projection of $\tilde{x}$ onto the y_A axis. Accounting for all the angular terms, the resulting projection is given as

$$\frac{\partial y_A(\tilde{x},t)}{\partial\tilde{x}}=\cos[\zeta(\tilde{x},t)]\cdot\cos[\beta(\tilde{x},t)]\cdot\sin[\phi(\tilde{x},t)]-\cos[\zeta(\tilde{x},t)]\cdot\sin[\beta(\tilde{x},t)]\cdot\cos[\phi(\tilde{x},t)]$$
$$\frac{\partial y_A(\tilde{x},t)}{\partial\tilde{x}}=\cos[\zeta(\tilde{x},t)]\cdot\sin[\phi(\tilde{x},t)-\beta(\tilde{x},t)] \tag{21}$$

In short, the cumulative effect of Eqs. (16–21) governs the sail motion in both time and space for the pitch and lead/lag case.

Pitch, Sweepback and Lead/Lag Case

The final case studied aims at modeling the global, three-dimensional motion of a sail blade. An obvious conclusion for the analysis, this case combines all 3 degrees of freedom under a single set of governing relations. All four angular terms, θ, ζ, ϕ, and β, are allowed to vary over time and space.

Following the same derivation procedure as for all the other cases, the result is almost the simple addition of the pitch and sweepback case with the pitch and lead/lag case. Only the governing equation for θ does not follow this general rule, because coupling between ζ, ϕ, and β also exists. A few more terms must therefore be added to the merger of Eqs. (13) and (16) to fully capture the variation of θ in the complete, three-dimensional case.

$$\left\{\rho\cdot\cos[\theta(\tilde{x},t)]\cdot\frac{\partial^2\theta(\tilde{x},t)}{\partial t^2}+\sigma_{\tilde{x}}(\tilde{x})\cdot\sin[\theta(\tilde{x},t)]\cdot\left(\frac{\partial\theta(\tilde{x},t)}{\partial\tilde{x}}\right)^2-\sigma_{\tilde{x}}(\tilde{x})\cdot\cos[\theta(\tilde{x},t)]\cdot\frac{\partial^2\theta(\tilde{x},t)}{\partial\tilde{x}^2}+\rho\cdot[\omega(\tilde{x},t)]^2\cdot\sin[(\theta(\tilde{x},t)]\cdot\cos^2[\theta(\tilde{x},t)]\cdot\cos^2[\zeta(\tilde{x},t)]-\frac{\partial\sigma_{\tilde{x}}(\tilde{x})}{\partial\tilde{x}}\cdot\cos[\theta(\tilde{x},t)]\cdot\frac{\partial\theta(\tilde{x},t)}{\partial\tilde{x}}\right\}+\left\{\rho\cdot\cos[\theta(\tilde{x},t)]\sin[\zeta(\tilde{x},t)]\frac{\partial^2\phi(\tilde{x},t)}{\partial t^2}-\rho\cdot\cos[\theta(\tilde{x},t)]\sin[\zeta(\tilde{x},t])\frac{\partial\omega(\tilde{x},t)}{\partial t}-2\rho\cdot\omega(\tilde{x},t)\cdot\sin[\theta(\tilde{x},t)]\cdot\cos^2[\theta(\tilde{x},t)]\cdot\cos^2[\zeta(\tilde{x},t)]\cdot\frac{\partial\phi(\tilde{x},t)}{\partial t}\right\}-\left\{\rho\cdot\sin[\theta(\tilde{x},t)]\cdot\cos^2[\theta(\tilde{x},t)]\cdot\left(\frac{\partial\zeta(\tilde{x},t)}{\partial t}\right)^2+2\rho\cdot\omega(\tilde{x},t)\cdot\cos[\theta(\tilde{x},t)]\cdot\sin^2[\theta(\tilde{x},t)]\cdot\cos[\zeta(\tilde{x},t)]\cdot\frac{\partial\zeta(\tilde{x},t)}{\partial t}\right\}+\left\{\rho\cdot\cos[\theta(\tilde{x},t)]\cdot\sin^2[\theta(\tilde{x},t)]\cdot\frac{\partial\phi(\tilde{x},t)}{\partial t}\cdot\frac{\partial\zeta(\tilde{x},t)}{\partial t}\cdot\{1+2\cos[\zeta(\tilde{x},t)]\}\right\}=0 \tag{22}$$

The first braces in Eq. (22) contains the terms that are common to both the pitch and sweepback case, and the pitch and lead/lag case. Terms in the second square brackets stem uniquely from the pitch and lead/lag case, whereas those in the third set of brackets stem from the pitch and sweepback case. Finally, the single expression in the fourth brackets represents the added coupling between sweepback and lead/lag.

Five additional equations of motion complement the governing equation for θ. As stated previously, this set of relations simply regroups the remaining governing equations from the past two cases. For completeness, these five equations are reiterated: Eqs. (14), (15), and (18–21). Together, these equations completely govern the three-dimensional motion of the sail blades.

Simulations and Results

Baseline Design

The baseline parameters of UltraSail, along with other relevant data used in the simulations, are summarized here, in Table 2.

Simulation: Numerical Methods

Although four sail blades are present in the baseline design for UltraSail, simulations were geared towards the motion of individual blades. Second-order finite differences [10] in both space and time were selected to numerically solve the sets of governing equations. Centered finite differences were used for points away from the edges, whereas most parameters at the boundary were solved using either

Table 2 UltraSail baseline parameters and data

Feature	Dimension
Number of blades, N	4
Blade length, L	5000 m
Blade chord, c	5 m
Blade thickness, $\bar{t}$	2 μm
Coated blade density, ρ	1430 kg/m^3
Mass of each blade, m_{sail}	71.5 kg
Mass of tip satellite, m_{sat}	32.1 kg
Thruster force	0.08 N
Thruster torque	0.2 N · m
Number of thrusters	2
Hub radius	2.5 m
Mass of hub $-$ M_{hub}, payload mass	1084 kg (1036 kg)
Separation between blade and spin axis, $\bar{x}_O$	2.5 m
Nominal solar pressure at 1 AU, P_o	9.1×10^{-6} Pa
Steady-state spin period, T	4272 s

forward or backward finite differences, accordingly. An exception to this general rule for the edges is θ, which was solved using the ghost-cell method [10,11] at the base of the blade.

Simulations were conducted as boundary-value and initial-value problems. Although an explicit method does exist for spatially dependent terms, the method was deemed too inaccurate with a second-order scheme. Steady-state cases were therefore handled iteratively. Time-dependent differentials, on the other hand, were handled in an explicit manner and did not experience significant inaccuracies, because convergence was observed towards known steady-state solutions.

Pitch-Only Case

As a simple first model, the steady-state pitch distribution of a straight, flat blade with a fixed 30 deg pitch at the tip and free boundary condition at the base was determined. Repeated tests indicated that computation time was only slightly affected by the tolerance level between successive iterations, but was significantly increased for smaller step sizes. As an even balance between computation time and accuracy, a step size of 31.25 m and a tolerance of 10^{-9}, defined as the acceptable relative variation in pitch between two successive iterations, were chosen:

$$\text{tolerance} \geq \left| \frac{\theta_{i+1}(\tilde{x}_j) - \theta_i(\tilde{x}_j)}{\theta_i(\tilde{x}_j)} \right| \tag{23}$$

These settings produced a pitch distribution with a maximum uncertainty of ± 0.8 deg at any given step, an acceptable margin of error.

Simulations of the time-varying blade shape followed these initial calculations. Three distinct boundary-condition scenarios were examined: fixed boundary conditions at both ends, fixed condition at the tip and free condition at the base, and fixed condition at the tip with matched viscous damping at the base. For the final scenario, the damping equation was similar to that proposed by Darmawijio et al. [12]. The same initial condition was applied to all three scenarios: an instantaneous acceleration in pitch of 0.33 deg/s^2 at the tip, with $\theta = 0$ deg along the entire length of the blade. The acceleration was calculated based on the thruster characteristics given in Table 2. Pitch at the tip was gradually changed from 0 to 30 deg in a span of 92 s, with a maximum angular velocity of 0.5 deg/s. After reaching 30 deg, the tip satellite was kept at 30 deg, hence the common fixed boundary condition at the tip for all three cases. For the scenario involving matched damping at the base, the ghost-cell method was used to calculate pitch at the base. A trial-and-error approach was taken to determine the ideal damping constant: $\alpha = (0.208 \pm 0.002)\ \text{N} \cdot \text{m} \cdot \text{s}$.

Simulations of the three scenarios conclusively demonstrated that matched damping at the hub was necessary to control the sail motion. Using this boundary condition, the sail was stabilized within 1 deg of its steady-state profile in about 1600 s, or 1/3 of the spin period. Other boundary conditions left residual oscillations in the sail. These alternate situations are quite undesirable, because pitch maneuvers must be controllable and often occur over short time spans. Figure 6 offers a sequence of pitch distributions as a function of lengthwise position and time. Pitch plots from all three scenarios taken at identical times are superimposed to show the significant difference between them. Interestingly, ripples in pitch are clearly observable for the incident wave. A quantitative assessment of the leading ripple was made for the match damping scenario. Its amplitude at the base of the blade was measured to be about 0.8 deg, which is small compared with the average sail pitch of 24.2 deg at that location and time.

Under ideal damping conditions, then, UltraSail could respond faster then other leading concepts, despite its much larger size. This remarkable result shows the promise of UltraSail, making it a very competitive alternative. Optimal responses are best achieved by initiating the maneuver at the blade tips and damping the propagating deflection waves at the base.

The space-dependent wave velocity along the sail blade was determined. A velocity profile was derived from both theory and numerical simulations. Agreement was found between the two results. From classical mechanics, the wave velocity is known to be dependent upon the coefficients of the space and time second derivatives in Eq. (11), respectively. For a straight, flat blade, linear stress is simply the sum of centrifugal force applied by individual sail elements and the tip satellite, divided by the cross-sectional area. Specifically then, the analytical expression for wave speed is given as

$$\bar{c}(\tilde{x}) = \sqrt{\frac{\frac{\rho\omega^2}{2}[(L+\bar{x}_O)^2 - \tilde{x}^2] + \frac{m_{\text{sat}}\omega^2}{c \cdot \bar{t}}(L+\bar{x}_O)}{\rho}} \tag{24}$$

Figure 7 provides a more vivid representation of the speed profile. For the dimensions and rates used in the simulations, the average wave speed was measured to be 6.40 m/s, which translates into a time of propagation along the entire blade of about 1/5 of the spin period (equivalent to about π radians of rotation). This lengthy travel time furthers the need for matched damping at the base to successfully implement rapid pitch maneuvers.

To complete the study of pitch-only cases, the assumption of uniform stress across the chord was evaluated. From literature [13], the longitudinal stress experienced by twisted, thin, rectangular sail blades is given by the following relation, accurate to second order:

$$\sigma_{\tilde{x}}(\tilde{x}, \tilde{y}, t) = Y \cdot \left[\varepsilon + \frac{1}{2} \cdot \left(\frac{\partial \theta(\tilde{x}, t)}{\partial \tilde{x}} \cdot \tilde{y} \right)^2 \right] \tag{25}$$

Assuming longitudinal stress uniform over the cross section is equivalent to assuming the previous chord-dependent term small relative to strain. For all three pitch-only models, the chord-dependent term was maximized at the tip. Scenarios involving a fixed or free boundary condition had this occurrence with the reflected pitch wave, 1600 s after the beginning of the maneuver, whereas the matched-damping case experienced its maximum with the outgoing pitch pulse a mere 11 s into the maneuver. The measured maximum magnitudes are presented:

$$\left| \frac{1}{2} \cdot \left(\frac{\partial \theta(\tilde{x}, t)}{\partial \tilde{x}} \cdot \tilde{y} \right)^2 \right|_{\max} = \{3 \times 10^{-5}|_{\text{fixBC}}\}; \{2.5 \times 10^{-3}|_{\text{freeBC}}\}; \{8 \times 10^{-6}|_{\text{dampedBC}}\} \tag{26}$$

Recalling that the expected average strain is 1.8×10^{-5} for UltraSail, the chord-dependent term in Eq. (25) has a comparable magnitude, even under matched-damping circumstances. The approximation that longitudinal stress remains constant over the chord is thus weak and limits the accuracy of the results. Nevertheless, the presented work offers a good first-order sense of the one-dimensional sail behavior.

Initial and Boundary Conditions for Multidimensional Models

A common situation was examined for simulations involving two or more dimensions of motion. The initial condition consisted of a sail blade constantly rotating at the baseline spin rate. The sail was set to operate with a steady-state sweepback deflection and linear acceleration away from the Sun at time 0. The remaining angles, θ, ϕ, and β, were assumed to be initially zero over the entire length of the blade, with an instantaneous acceleration in pitch of 0.33 deg/s^2 at the tip. A pulselike pitch profile was applied at the tip, with a 30 deg amplitude and maximum velocity of 0.5 deg/s. The pulses were designed to last about 1/10 of a full spin rotation (equivalent to roughly 427 s) and provide an overall lead deflection without changing the long-term spin velocity and acceleration. The applied pitch profile is shown in Fig. 8. As discussed in later sections, various damping conditions were tested at the base, but only damping in pitch was retained. All the simulations were conducted on a Toshiba satellite computer with a 1.5 GHz Intel Centrino processor and 512 MB of RAM.

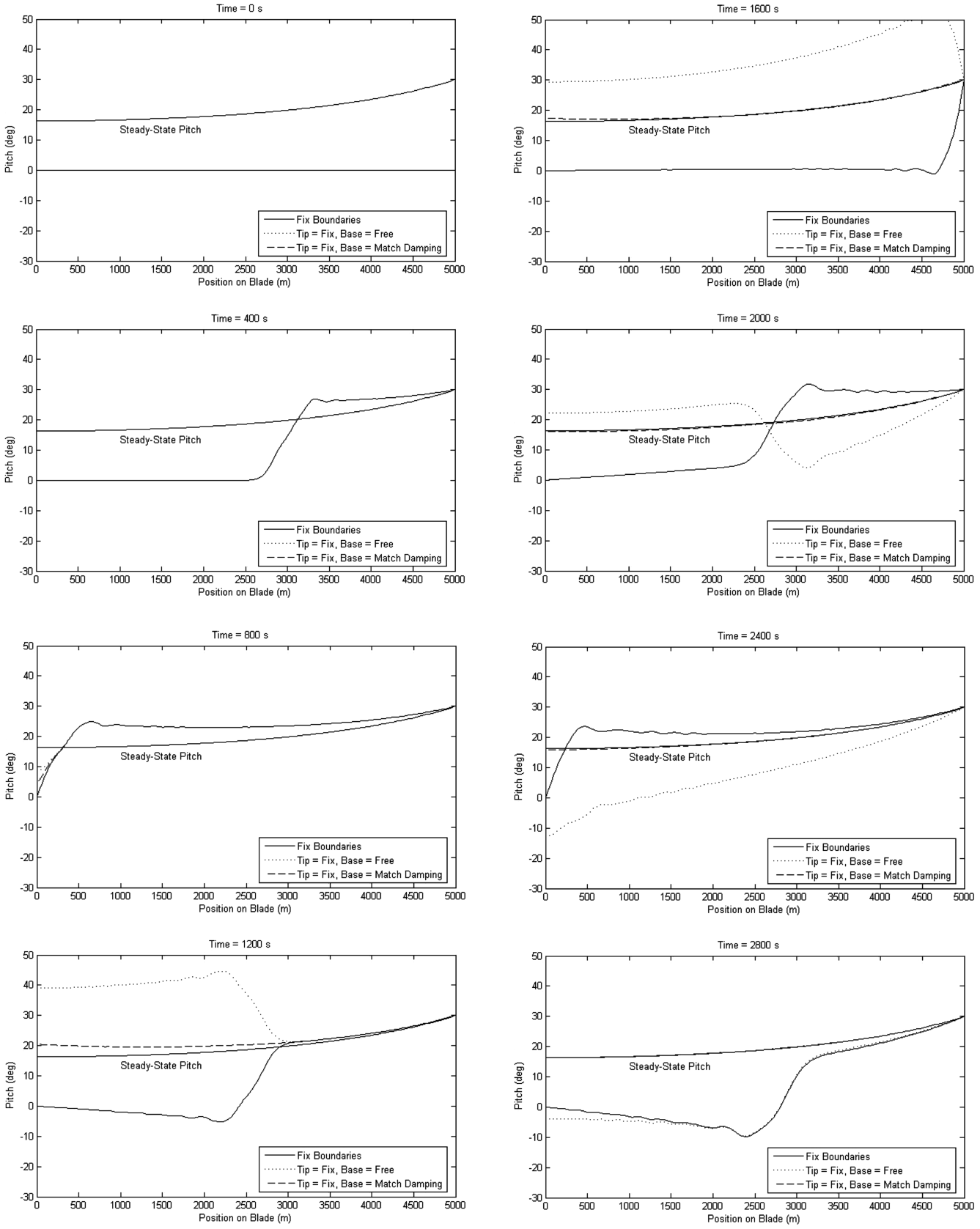

Fig. 6 Superposition of the transient pitch distribution from three separate scenarios. Images are placed in chronological order, from t = 0 to 2800 s.

Pitch and Sweepback Case

Starting on similar grounds to the pitch-only case, the steady-state sweepback solution was considered first. Two solutions, one analytic and one iterative, were determined. The analytic solution was founded on two additional assumptions to the five stated at the outset of the theory: the longitudinal stress equaled that of a straight, flat blade, and small-angle approximations for ζ were valid. Recalling the force balance equation along the z_O axis for the pitch and sweepback case, Eq. (14), the linear stress term can be replaced by the expression for that of a straight, flat blade:

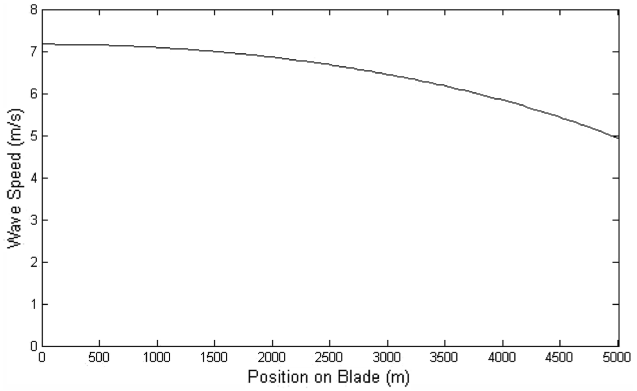

Fig. 7 Pitch-wave speed profile over the sail blade length.

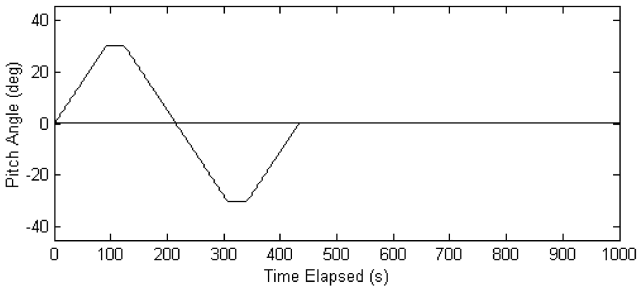

Fig. 8 Satellite-controlled input pitch profile.

$$\rho \cdot a_z = \left(\frac{\rho\omega^2}{2}[(L+\bar{x}_O)^2 - \tilde{x}^2] + \bar{T}\right)\frac{\mathrm{d}\sin[\zeta(\tilde{x})]}{\mathrm{d}\tilde{x}} - \rho\omega^2\tilde{x}\sin[\zeta(\tilde{x})] + \frac{P_{\text{solar}}}{\bar{t}}\cos[\zeta(\tilde{x})] \tag{27}$$

The symbol $\bar{T}$ represents the tension applied by the tip satellite.

$$\bar{T} = \frac{m_{\text{sat}}}{c\cdot\bar{t}}\sqrt{a_z^2 + [\omega^2(L+\bar{x}_O)]^2} \tag{28}$$

Replacing $\sin[\zeta(\tilde{x},t)]$ with $dz_O(\tilde{x})/d\tilde{x}$, P_{solar} with its equivalent expression in Eq. (12), and applying small-angle approximation renders a linear ordinary differential equation (ODE). Because the equation is of second order, two boundary conditions are necessary. Setting the fixed z_O position at the base of the sail blade equal to zero provides a first, trivial condition. The second, physical in nature, ensures that the hub and central payload accelerate away from the Sun at the same rate as the sail and tip satellite. Upon solving the ODE and applying both boundary conditions, an approximate, analytical solution for sweepback deflection as a function of position along the blade is obtained:

$$z_O(\tilde{x}) = \frac{M_{\text{hub}}a_z}{\omega N c\bar{t}}\sqrt{\frac{2}{\rho[\frac{\rho\omega^2}{2}(L+x_o)^2+\bar{T}]}} \cdot \operatorname{arctanh}\left(\frac{\omega\rho\cdot\tilde{x}}{\sqrt{2\rho[\frac{\rho\omega^2}{2}(L+x_o)^2+\bar{T}]}}\right) - \frac{\rho a_z - \frac{P_o}{\bar{t}}}{\rho\omega^2} \cdot \ell_n\left(\frac{\rho\omega^2}{2}[(L+x_o)^2-\tilde{x}^2]+\bar{T}\right) - \bar{z}_O \tag{29}$$

The constant of integration $\bar{z}_O$ sets the zero sweepback point to be at the base of the blade:

$$\bar{z}_O = \frac{M_{\text{hub}}a_z}{\omega N c\bar{t}}\sqrt{\frac{2}{\rho[\frac{\rho\omega^2}{2}(L+x_o)^2+\bar{T}]}} \cdot \operatorname{arctanh}\left(\frac{\omega\rho\cdot x_o}{\sqrt{2\rho[\frac{\rho\omega^2}{2}(L+x_o)^2+\bar{T}]}}\right) - \frac{\rho a_z - \frac{P_o}{\bar{t}}}{\rho\omega^2} \cdot \ell_n\left(\frac{\rho\omega^2}{2}[(L+x_o)^2-x_o^2]+\bar{T}\right) \tag{30}$$

Equation (29) differs from our past results [4] by accounting for linear acceleration away from the Sun and treating the blade as a continuous membrane instead of a point mass with an effective arm length.

The iterative solution, on the other hand, accounted for all realistic constraints, such as a fixed blade length, exact longitudinal stress distribution, and trigonometric terms. Two distinct projections of the force balance equation, along the z_O and x_O directions, led to additional necessary relations:

$$\sigma_{\tilde{x}}(\tilde{x})\cdot\frac{\partial\zeta(\tilde{x})}{\partial\tilde{x}} + \frac{P_{\text{solar}}}{\bar{t}} = \rho\cdot\{a_z\cos[\zeta(\tilde{x})] + \omega^2\cdot x_O\sin[\zeta(\tilde{x})]\} \tag{31}$$

$$\frac{\partial\sigma_{\tilde{x}}(\tilde{x})}{\partial\tilde{x}} = \rho\cdot\{a_z\sin[\zeta(\tilde{x})] - \omega^2\cdot x_O\cos[\zeta(\tilde{x})]\} \tag{32}$$

Equation (31) was used to iterate the value of ζ over the length of the blade, whereas Eq. (32) served as a tool to calculate the exact linear stress. The same two boundary conditions as for the analytical solution were applied. The complete computational procedure consisted of using the approximate, analytic solution as the initial guess solution and running through two convergence loops, one containing Eq. (31), embedded into the other, containing Eq. (32), until stress, linear acceleration, and sweepback deflection agreed within a tolerance of 10^{-9}. The iteratively determined blade shape and the difference in calculated sweepback deflection between the analytical and iterative approaches are plotted here, in Fig. 9.

As made obvious by the plotted shapes, both solutions are nearly identical. Their minimal divergence is attributable to the inclusion of three effects in the iterative solution that are not accounted for in the analytic solution: the dependence of longitudinal stress on linear acceleration of the sail away from the Sun, the nonlinear distribution of radial distance from the spin axis over the blade length, and the component of the solar pressure along x_O. The divergence is most noticeable towards the tip of the sails, where tension is at a minimum. Variations in stress can thus be expected to be small, which corroborates the assumption of constant stress for time-dependent simulations. According to the numerical results, UltraSail blades would carry a maximum deflection of 547 m, occurring at 4500 m from their respective blade base, and a maximum sweepback angle of 12.8 deg when at equilibrium. Figure 9 conclusively demonstrates that the analytical equation for the steady-state sweepback shape approximates numerical simulations virtually flawlessly.

Given the strong similarity between both predicted sweepback shapes, it is noteworthy to compare the steady-state linear acceleration away from the Sun obtained through each approach. On the analytical front, an equation for a_z was obtained by combining the projection of the sail tension at the tip along the z_O direction with the derivative of Eq. (29):

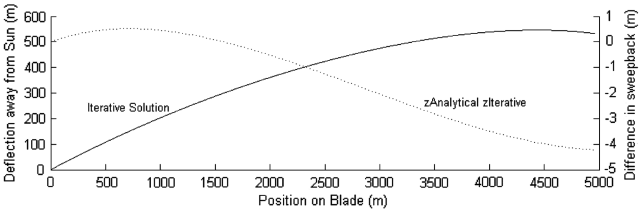

Fig. 9 Steady-state shape of a sweptback sail and relative difference in calculated sweepback deflection between the analytical and iterative solutions.

$$a_z = \frac{P_o \cdot L \cdot c}{m_{\text{sail}} + \frac{M_{\text{hub}}}{N} + m_{\text{sat}}} \tag{33}$$

Equation (33) predicts a linear acceleration of 0.607 mm/s^2 for the baseline design. This encouraging result is relatively close to the iterative solution of 0.592 mm/s^2; both results differ only by 2.5%. Thus, for similar UltraSail designs operating at steady-state conditions, Eq. (33) provides a reasonable estimate of the linear acceleration away from the Sun. Given the baseline-design payload mass of 1036 kg cited in Table 2, these results promote UltraSail as a leading candidate for midterm missions [1]. It not only matches most hopeful characteristic accelerations (accelerations at 1 AU), it does so with a much higher payload mass. Thus, for more conservative mission requirements, UltraSail could be an attractive candidate with a much shorter blades than its baseline design.

The transient blade deflection induced by a pitch maneuver was modeled next. The governing relations for the pitch and sweepback case, along with the restriction of a fixed blade length, were combined within a single program. Initial and boundary conditions for multidimensional models described in the past section were applied. Through a trial-and-error approach, the optimal damping coefficient for pitch deflections was determined to be identical to that of the one-dimensional model, but with a greater uncertainty: $\alpha = (0.208 \pm 0.008)\ \text{N} \cdot \text{m} \cdot \text{s}$. This suggests little to no correlation between the various degrees of freedom. However, small, but noticeable reflected waves continued to be observed under ideal damping conditions. Damping for sweepback deflection at the base was therefore considered. Despite numerous tests and designs, no ideal, matched-damping conditions for ζ were found. Fortunately, wavelike fluctuations in sweepback were observed to be relatively small (see Figs. 10 and 11). Little damping would therefore be necessary to completely eliminate transient oscillations in the sail. Because physical waves typically travel along the length of their medium and the sweepback angle continuously changes in time-dependent simulations, appropriate dampers would likely need to be two dimensional. Given the limited success of the attempted damping schemes, no further conclusive remarks can be made on the topic.

Plots of the initial, steady-state sweepback sail shape and deviations from this equilibrium as a function of lengthwise position over a period of 2800 s are given in [10] and Fig. 11. The computation time required to produce the data for these plots, with step sizes of 1 s in time and 31.25 m in space, was 327 s. Interesting behaviors were observed from the generated results. First, the initial pitch pulses tend to spread and smooth as they move towards the hub. This flattening effect is because of the velocity increase towards the base of the blade, as highlighted in Fig. 7, which accelerates the leading edge of the pulses relative to the trailing edge. Also, pitch pulses and consequent transient displacements in sweepback traveled down the blade at identical speeds. Theory supports this finding, because the coefficients for the second-order partial derivatives in space and time of z_O, Eq. (14), are identical to those for θ, Eq. (13). This equivalence in velocity demonstrates that the sail exhibits no preference in transmitting a certain type of time-dependent deflection over another. Last, the chord-dependent term of longitudinal stress, Eq. (25), had a maximum of 1.7×10^{-5} occurring at the base of the sail and at time 1154 s. This again indicates that the overriding approximation of uniform stress is valid only to first order. As an upper limit for the response of UltraSail to a pair of 30 deg pulses at the tip, the maximum displacement from the initial, steady-state blade shape was simulated to be 93.5 m, which occurred 4875 m from the sail blade base and 1766 s after the maneuver began.

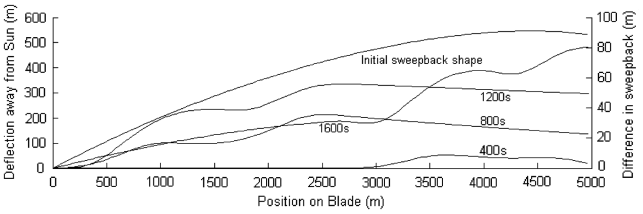

Fig. 10 Steady-state shape of a sweptback sail and transient sweepback displacement from equilibrium as a function of position along the blade taken at four different times: 400, 800, 1200, and 1600 s.

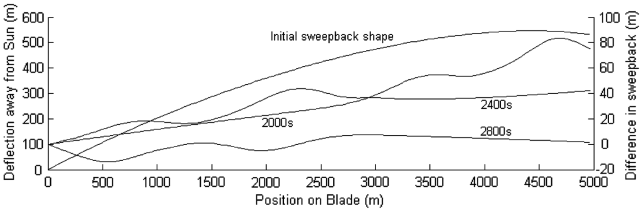

Fig. 11 Steady-state shape of a sweptback sail and transient sweepback displacement from equilibrium as a function of position along the blade taken at three different times: 2000, 2400, and 2800 s.

Pitch and Lead/Lag Case

Because steady-state motion does not involve lead/lag (i.e., $\phi = 0$ deg over the entire blade length), no steady-state models of the pitch and lead/lag case were made. Instead, only transient motion was examined. Variables ϕ, β, θ, y_A, and x_A were explicitly calculated over both space and time. The initial steady-state sweepback deflection of the sail was assumed to remain unchanged over time. Therefore, variables ζ and z_O were kept constant throughout the simulations.

The first series of simulations exhibited strong divergence over time. All the variables, particularly θ, developed spatial fluctuations that grew uncontrollably. These large, unphysical ripples are demonstrations of "ringing." Under such unwanted circumstance, numerical inaccuracies become dominant for a system and cause near-random values for all system parameters. After careful research, the source of the divergence was narrowed to the partial spatial derivative of $\sin[\phi(\tilde{x}, t)]$ in Eq. (17). It was first to demonstrate strong oscillations during the simulations, when the angle ϕ approached 0 deg.

A mathematical, ad hoc solution to counter this numerical problem consists of truncating part of Eq. (21)

$$\frac{\partial y_A(\tilde{x}, t)}{\partial \tilde{x}} \approx \cos[\zeta(\tilde{x}, t)] \cdot \cos[\beta(\tilde{x}, t)] \cdot \sin[\phi(\tilde{x}, t)] \tag{34}$$

As demonstrated by Botter [10], Eq. (34) ensures that ϕ is dominated by β instead of numerical errors when it nears 0. It also holds similarities with artificial damping [14,15], a numerical technique used in fluid dynamics. The induced error is best evaluated by considering the maximum absolute difference in the spatial derivative of $\sin[\phi(\tilde{x}, t)]$ between the approximate and exact solutions [10]:

$$\Delta\left(\frac{\partial \sin[\phi(\tilde{x}, t)]}{\partial \tilde{x}}\right)\bigg|_{\max} = \sec^2[\beta(\tilde{x}, t)] \cdot \frac{\partial \beta(\tilde{x}, t)}{\partial \tilde{x}} \tag{35}$$

Over the 2800-s time frame of the simulations, β remains within 4 deg of the steady-state solution, and the average magnitude of its partial derivative with respect to $\tilde{x}$ is about 10^{-4}. The absolute error, therefore, seldom exceeds 1.005×10^{-4}. This demonstrates that the yielded simulations are relatively close to the actual, anticipated sail motion. For further details on the proposed solution and its numerous characteristics, see [10].

Numerically stable simulations of the sail motion for the pitch and lead/lag case followed. Trial and error was again used to optimize the characteristics of the damper. The same damping coefficient as in the pitch and sweepback case was deemed optimal: $\alpha = (0.208 \pm 0.008)\ \text{N} \cdot \text{m} \cdot \text{s}$. However, significant reflected waves remained. Speculations are that a two-dimensional damping system would be necessary to contend with these deflections along the spin plane. For the simulations, therefore, the variable y_A was permanently set equal to 0 at the blade base, whereas ϕ was allowed to vary. Images of the lead/lag distributions over the blade length at different time increments are presented in Figs. 12 and 13.

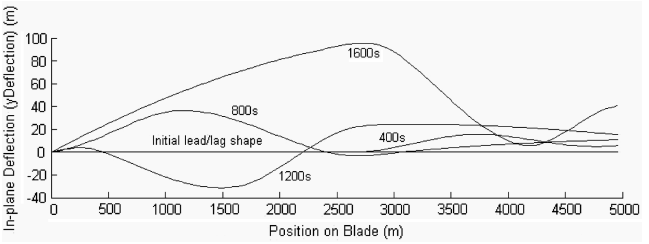

Fig. 12 Steady-state lead/lag shape of a sail and transient in-plane displacement from equilibrium as a function of position along the blade taken at four different times: 400, 800, 1200, and 1600 s.

Fig. 13 Steady-state lead/lag shape of a sail and transient in-plane displacement from equilibrium as a function of position along the blade taken at three different times: 2000, 2400, and 2800 s.

The expected final steady-state shape is relatively trivial: the sail should deflect upwards with a constant angle β. However, because of the fixed boundary condition for y_A, the blade never achieved this state during the simulations. Instead, large traveling waves were witnessed, as can be observed in the plots shown here. Just as with the pitch and sweepback case, flattening of the pitch pulses occurred because of the increase in velocity towards the spin axis.

Another interesting phenomenon is the variation in spin velocity, and consequently angular acceleration, as a function of position along the blade. This particularity is mainly caused by three factors: the finite amount of time it takes for pitch pulses to travel through the sail, the nonuniformity of transient pitch angles, and the tendency of solar pressure force to produce larger angular accelerations at smaller distances from the spin axis. Additionally, the spin rate was also time dependent in this simulation, which consequently affected the wave speed. Nevertheless, the sail retained its property of unpreferred wave type, because the propagation speed for both pitch and lead/lag was identical.

The propagating lead/lag wave also appeared to grow upon reflecting from the sail base because of the lack of damping. Following a similar reflection at the tip, the sail was observed to quickly accelerate the tip satellite upwards, in the direction of the initial lead deflection. This odd behavior was determined not to be a numerical issue. It may, however, be an artifact of the basic assumptions on which the equations of motion were derived, or from the strict and perhaps unrealistic conditions at the ends. Whatever the reason, it remains an intriguing behavior that needs to be better understood to successfully control applied maneuvers on UltraSail.

Last, a few numerical results are stated to place the qualitative findings in context. For a 2800-s long simulation, with step sizes of 1 s in time and 31.25 m in space, the designed program required 487 s of computation time. Unsurprisingly, the maximum deflection caused by lead/lag occurred at the tip, with a magnitude of 281 m and at time 2800 s. Although this deflection is large, it is less than 6% of the blade length, and given the ultralight weight of the sail material, it requires little energy. The largest angular deflection in β was just under 7 deg, recorded at 125 m from the base of the blade and 2664 s after the initial perturbation. Finally, the assumption of uniform stress over the chord was again deemed valid only to first order, because the chord-dependent term in Eq. (25) had a maximum value of 2.1×10^{-5}, which took place 1154 s into the maneuver at the base.

Pitch, Sweepback, and Lead/Lag Case

As it was when developing the underlying theory, this three-dimensional case is a synthesis of the pitch and sweepback case with the pitch and lead/lag case. The methods, approximations, boundary and initial conditions, and numerical procedures used for the past two cases were grouped into a single, unified program to simulate the translational and rotational motion along all three Cartesian directions of a sail blade. Matched damping for pitch pulses was also included in the simulations, with the same damping constant as before: $\alpha = (0.208 \pm 0.008)\ \mathrm{N \cdot m \cdot s}$. Because no appropriate boundary damping conditions were found in the past two sections for translational motion, other variables were kept constant at the base throughout the simulations, namely $z_O = z_A = 0$, $y_A = 0$ m, and $x_A = 0$ m. The remaining variables were allowed to change over space and time. Their respective values were explicitly iterated using the complete set of governing equations. As described in the past section, the divergence generated by rounding errors was handled through an ad hoc approximation for the definition of ϕ.

Plots of the pitch angle, sweepback, and lead/lag deflections as a function of lengthwise position and time are shown here, in Figs. 14–17. The most astonishing results are the remarkably close similarities

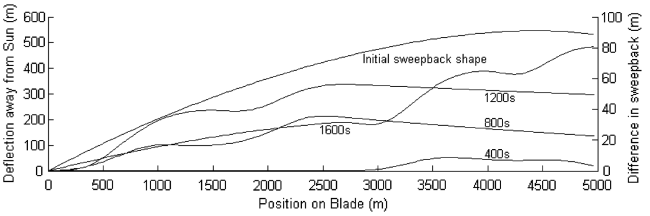

Fig. 14 Steady-state shape of a sweptback sail and transient sweepback displacement from equilibrium as a function of position along the blade taken at four different times: 400, 800, 1200, and 1600 s.

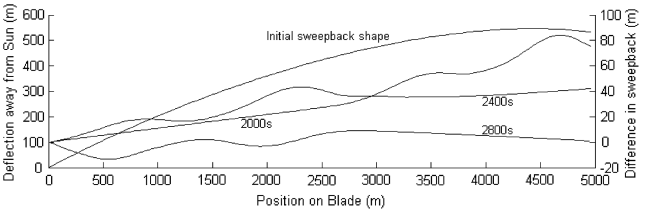

Fig. 15 Steady-state shape of a sweptback sail and transient sweepback displacement from equilibrium as a function of position along the blade taken at three different times: 2000, 2400, and 2800 s.

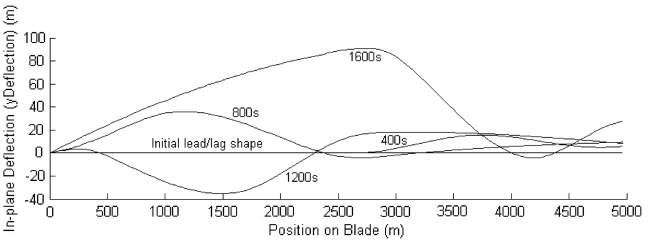

Fig. 16 Steady-state lead/lag shape of a sail and transient in-plane displacement from equilibrium as a function of position along the blade taken at four different times: 400, 800, 1200, and 1600 s.

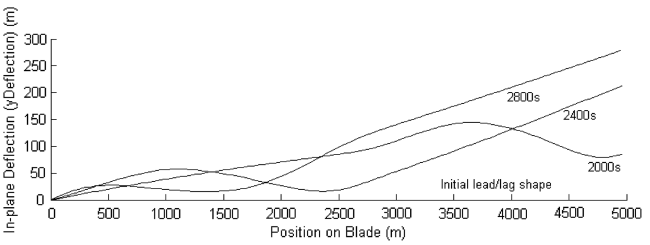

Fig. 17 Steady-state lead/lag shape of a sail and transient in-plane displacement from equilibrium as a function of position along the blade taken at three different times: 2000, 2400, and 2800 s.

Table 3 Recorded data at the randomly selected time of 2399 s and position of 3718 m from the base

Cartesian coordinates	Pitch and sweepback	Pitch and lead/lag	Pitch, sweepback, and lead/lag
x_A	3686 m	3674 m	3680 m
y_A	——	−113.6 m	−103.4 m
z_A	488.6 m	——	488.8 m

between these plots and the combination of those shown for the pitch and sweepback, and the pitch and lead/lag cases. Table 3 provides evidence. Relative differences for all three Cartesian directions are less than 9%, with x_A carrying the smallest difference of about 0.2%. These results conclusively demonstrate that the interdependence between sweepback and lead/lag has a minimal effect on the sail motion. The global sail motion for complex scenarios can be thus reasonably modeled by treating sweepback and lead/lag separately and superimposing them afterwards. Equivalently, if only two-dimensional motion is considered, the third dimension can be dropped without significantly altering the expect behavior. In both instances, the needed computation time may be reduced.

Because of this comparability, the qualitative results for the pitch, sweepback, and lead/lag case are basically the sum of the results found in the past two sections. For completeness, these common properties are repeated next in succinct fashion:

1) Pitch pulses tended to spread because of the variation in traveling speed between the leading and lagging edges.

2) All types of waves (pitch, sweepback, and lead/lag) propagated at the same rate.

3) The spin deflection, defined by both β and ϕ, was both space and time dependent. It grew unevenly over space and relatively steadily as time evolved.

4) The tip satellite was again abruptly accelerated by the large, reflecting lead deflection. Its motion was therefore quite discontinuous with sporadic boost and periods of little to no accelerations.

5) The assumption of an even longitudinal stress distribution over the chord was found valid to first order only, with a maximum of 2.1×10^{-5} for the chord-dependent term in Eq. (25). This maximum occurred at the base, at time 1152 s.

To complete the statement of findings for this final case, a few numerical results are outlined. Over the first 2800 s of the transient sail motion, the maximum sweepback deflection from the initial steady state shape was 90.5 m, which occurred at 4875 m from the base of the blade and at time 1766 s. The upper limit for lead/lag occurred at the tip, with a measured deflection of 266.7 m at time 2800 s. Both of these are small compared with their lengthwise position, with displacements of about 9 and 5%, respectively, relative to their x_A location. The largest angular deflections recorded were little under 7 deg for β, taking place 2667 s after the initial perturbation and 125 m away from the hub, and about 8 deg for ζ, recorded at the tip and at time 1892 s. Finally, the computation time given the same step sizes as for the two-dimensional cases, $\Delta t = 1$ s and $\Delta x = 31.25$ m, was 726 s.

Conclusions

The nonlinear governing equations of motion for spin-stabilized solar sails have been derived from structural mechanics principles. Four cases in particular were considered, extending from a single dimension to a complete three-dimensional model. The developed theory was shown to relate to known linear equations of motion for the heliogyro type of spinning solar sails. The governing equations were applied to simulate the stationary and dynamic characteristics of UltraSail blades. Results indicated that the underlying assumption of uniform longitudinal stress over the chord was valid to a first order only.

Analytical expressions for the steady-state sweepback position and acceleration were found. Both were shown to match the numerical result obtained from iterative calculations nearly perfectly. Under steady-state travel, with sails fully exposed to the Sun and rotating at a fixed angular velocity, UltraSail can be expected to maintain a large acceleration, whereas its blades maintain a certain camber away from the Sun. For the baseline design considered, UltraSail is predicted to have an acceleration of about 0.6 $\mathrm{mm/s^2}$ and a maximum camber deflection of 547 m at 1 AU. With such predicted performances, UltraSail meets and exceeds the characteristic properties of midterm solar sail missions.

For transient cases, simulations revealed important facts and uncommon behaviors. First, matched damping was demonstrated to be necessary to perform control maneuvers quickly and accurately. Results from the pitch-only, one-dimensional case indicated that UltraSail could outperform leading solar sail designs, in terms of response time. In wake of this finding, the use of tip satellites to initiate maneuvers was deemed essential to minimize the response time. The velocity profile was also presented for the one-dimensional case. Pitch waves, traveling along the blade length, accelerated towards the spin axis and were consequently observed to flatten. The same observation was made for two- and three-dimensional models. Sails were shown, both numerically and theoretically, to carry all types of wave at the same speed under all conditions. Spin velocity grew fastest near the hub and steadily, on average, over time in scenarios in which spin was made dependent on both space and time. This caused the tip satellite to experience uneven spin acceleration, with periodic large accelerations to deflect it within the spin plane.

Comparison between the two-dimensional models and the three-dimensional one revealed that the interdependence between sweepback and lead/lag only minimally impacts the sail motion. Therefore, for complex problems or situations in which interest is geared toward only two dimensions, the two-dimensional simulations provide a reasonable approximation for the expected three-dimensional behavior, while likely reducing the computation time.

Acknowledgment

The authors would like to thank Philippe Geubelle for his contribution to the elaboration of the first governing equation and for providing key information on the development of finite-difference routines.

References

[1] McInnes, Colin, "Solar Sailing: What Are We Waiting for?," *Solar Sail Technologies and Applications Conference*, NASA/GSFC, Greenbelt, MD, Sept. 2004.

[2] Leipold, M., Fichtner, H., Heber, B., Groepper, P., Lascar, S., Burger, F., Eiden, M., Niederstadt, T., Sickinger, C., Herbeck, L., Dachwald, B., and Seboldt, W., "Heliopause Explorer: A Sailcraft Mission to the Outer Boundaries of the Solar System," *Acta Astronautica*, Vol. 59, Nos. 8–11, Oct.–Dec. 2006, pp. 785–796. doi:10.1016/j.actaastro.2005.07.024

[3] Mitsugi, J., Natori, M., and Miura, K., "Preliminary Evaluation of the Spinning Planar Solar Sail," AIAA Paper 1987-742, 1987, pp. 135–142.

[4] Burton, R. L., Coverstone, V. L., Ertmer, K. M., Hargens-Rysanek, J., Botter, T., Benavides, G., Woo, B., Carroll, D. L., Gierow, P. A., Farmer, G., and Cardin, J., "UltraSail:Ultra-Lightweight Solar Sail Concept," *41st AIAA/ASME/SAE/ASEE Joint Propulsion Conference and Exhibit*, AIAA Paper 2005-4117, Tucson, AZ, July 2005.

[5] MacNeal, R. H., "The Heliogyro: An Interplanetary Flying Machine," NASA ARC-R-249, March 1967.

[6] MacNeal, R. H., "Structural Dynamics of the Heliogyro," NASA CR-1745, May 1971.

[7] Salama, M., and Trubert, M., "Second Order Nonlinear Equations of Motion for Spinning Highly Flexible Line Elements," AIAA Paper 1979-736, 1979, pp. 86–93.

[8] Johnson, L., "Propulsion Technologies for Exploration of the Solar System and Beyond (Plenary)," *Review of Scientific Instruments*, Vol. 73, No. 2, Feb. 2002, pp. 1079–1082. doi:10.1063/1.1431426

[9] Hall, J., Glaese, R., and Flint, E., "Dynamic Behavior of Thin Film Membrane Strips," *43rd AIAA/ASME/ASCE/AHS/ASC Structures,*

Structural Dynamics, and Materials Conference, AIAA Paper 2002-1378, Denver, CO, April 2002.

[10] Botter, T., "Structural Dynamics of UltraSail: A Spin-Stabilized, Mast-Free Solar Sail Design," M.S. Thesis, Aerospace Department, University of Illinois at Urbana–Champaign, Urbana, IL, 2006, pp. 55–59.

[11] Dadone, A., and Grossman, B., "Ghost-Cell Method for Inviscid Two-Dimensional Flows on Cartesian Grids," *AIAA Journal*, Vol. 42, No. 12, 2004, pp. 2499–2507.

[12] Darmawijio, Van Horssen, W. T., and Clement, P., "On a Rayleigh Wave Equation with Boundary Damping," *Nonlinear Dynamics*, Vol. 33, No. 4, 2003, pp. 399–429. doi:10.1023/B:NODY.0000009939.57092.ad

[13] Green, A. E., "The Equilibrium and Elastic Stability of a Thin Twisted Strip," *Proceedings of the Royal Society of London A*, Vol. 154, No. 882, 1936, pp. 430–455. doi:10.1098/rspa.1936.0061

[14] Efraimsson, G., "A Numerical Method for the First-Order Wave Equation with Discontinuous Initial Data," *Numerical Methods for Partial Differential Equations*, Vol. 14, No. 3, 1998, pp. 353–365. doi:10.1002/(SICI)1098-2426(199805)14:3<353::AID-NUM5>3.0.CO;2-L

[15] Efraimsson, G., "A 2-D Analysis of the Influence of Artificial Viscosity Terms on Solutions of the Euler Equations," *Journal of Computational Physics*, Vol. 138, No. 1, 1997, pp. 103–120. doi:10.1006/jcph.1997.5828